# Kinetic phenomena of helical plasma waves with orbital angular momentum

D. R. Blackman, <sup>1, 2, \*)</sup> R. Nuter, <sup>2</sup> Ph. Korneev, <sup>3</sup> A. Arefiev, <sup>1</sup> and V.T. Tikhonchuk<sup>2, 4</sup>

- <sup>2)</sup> CELIA, University of Bordeaux, CNRS, CEA, 33405 Talence, France
- <sup>3)</sup>P. N. Lebedev Physics Institute, Russian Academy of Sciences, 119991 Moscow, Russia
- <sup>4)</sup> ELI-Beamlines Center, Institute of Physics, Czech Academy of Sciences, 25241 Dolní Břežany, Czech Republic

An accurate description of plasma waves is fundamental for the understanding of many plasma phenomena. It is possible to twist plasma waves such that in addition to having longitudinal motion, they can possess a quantized orbital angular momentum. One such type of plasma wave is the Laguerre-Gaussian mode. Three-dimensional numerical particle-in-cell simulations demonstrate the existence of stable long-lived plasma waves with orbital angular momentum. These waves can be shown to create large amplitude static magnetic fields with unique twisted longitudinal structures. In this paper we review the recent progress in studies of helical plasma waves and present a new analytical description of a standing Laguerre-Gaussian plasma wave mode along with 3D PIC simulation results. The Landau damping of twisted plasma waves shows important differences compared to standard longitudinal plasma wave Landau damping. These effects include an increased damping rate, which is affected both by the focal width and the orbital number of the plasma wave. This increase in the damping rate is of the same order as the thermal correction. Moreover, the direction of momentum picked up by resonant particles from the twisted plasma wave can be significantly altered. By contrast the radial electric field has a subtle effect on the trajectories of resonant electrons.

<sup>&</sup>lt;sup>1)</sup>Mechanical and Aerospace Engineering, University of California San Diego, 9500 Gilman Drive, La Jolla, CA 92093-0411, USA

<sup>\*)</sup>For correspondence: drblackman@eng.ucsd.edu

## I. INTRODUCTION

For some time now it has been known that light waves in a specific configuration can carry orbital angular momentum and that this property can be transferred to objects it interacts with<sup>1</sup>. These light waves, which can be described using a Laguerre-Gaussian solution to the paraxial wave equation, often referred to as either helical waves or vortex waves somewhat interchangeably, have been suggested for use in a variety of applications at low intensities<sup>2</sup>.

More recently there have been several advances in optical and experimental techniques that have allowed production of these beams near or at relativistic intensities via spiral staircase-like mirrors<sup>3,4</sup> and transmissive phase plates<sup>5–7</sup>. A fundamental phenomena when considering laser-plasma interactions is the electron plasma wave, which is also able to be constructed in helical configurations. While a helical plasma wave described by a Laguerre-Gaussian paraxial solution has previously been proposed<sup>8,9</sup>, the solutions to the dispersion and Landau damping rate in the linear regime were incomplete. A more accurate solution of the dispersion equation for the helical plasma waves, along with kinetic calculations that demonstrate the stability of such waves, is presented in Ref. 10. There are further works on the properties of plasma waves with orbital angular momentum<sup>11–13</sup> however the conclusions drawn in these studies are based on the incomplete previously described<sup>9</sup> plasma wave dispersion and Landau damping. These results could be revisited using the methodology described in this article and may result in further insights.

Helical laser produced plasma waves are important for a number of applications, an example being the generation of extreme intensity ultra-short helical pulses through processes like stimulated Raman amplification<sup>14–17</sup>. A particular nomenclature of "light-spring" <sup>18</sup> has been previously used to denote a multi-colored laser beam with an azimuthal mode index correlated to the laser wavelength, configured such that it generates helical backscatter as a result of stimulated Raman scattering. The Raman backscatter instability can be used to generate high amplitude plasma waves<sup>16</sup>. A mechanism has been proposed where two copropagating laser beams with opposing helicity produce a ponderomotive force that excites a helical plasma wave<sup>19</sup>. Such plasma wave was suggested for generation of large longitudinal magnetic fields from azimuthal currents, which are a general feature of helical plasma waves<sup>10</sup>. While there is a number of applications including helical plasma waves, a further investigation of the basic physics is of interest, in particular, in the non-linear Landau

damping regime in the high energy density plasmas, where plasma wave dynamics are shown to be dominated by kinetic effects<sup>20</sup>, and where the study of helical plasma waves remains unexplored.

This article presents an extended summary of physics of helical plasma waves and related processes based on the kinetic consideration, as described in Refs. 10, 21, and 22 along with new analytical and numerical results including three-dimensional particle-in-cell (PIC) simulations. The new results include an analytical description of the second order magnetic fields associated with standing helical plasma waves which is presented in Section III). To support the analytical results, 3D PIC simulations of a standing helical plasma wave with l=2 and a traveling plasma wave with l=1 are shown in comparison to the previously produced traveling l=2 mode. Additionally Section IV presents an exploration of the trajectories of single particles within plasma wave electric fields, demonstrating the constraining effect of the radial electric field upon populations of resonant electrons. Finally in Section V several further insights into the non-linear damping of helical plasma waves are presented.

This paper addresses three topics: the first is an overview of a self-consistent solution to the dispersion and damping of helical plasma waves in the linear regime (Section II); the second being the generation of magnetic fields via the second order vector field (Section III); the third being the transfer of momentum from helical plasma wave to resonant electrons (Section IV) through the nonlinear Landau damping (Section V).

# II. LAGUERRE-GAUSSIAN PARAXIAL SOLUTION FOR PLASMA WAVES AND A SELF-CONSISTENT LANDAU DAMPING

This section provides a brief overview of the dispersion and Landau damping of helical plasma waves in the linear regime presented in Ref. 21. We consider the long wavelength limit of  $k\lambda_D \ll 1$  in the calculation detailed below, such that the non-linear strong damping case is explicitly excluded in the linear analysis. The reasoning behind this consideration is that the plasma wave dispersion and damping can be described analytically as small corrections to the plasma frequency. This also facilitates a comparison with numerical simulations. The key to the solution lies within the paraxial approximation to the wave equation and so the initial steps will be detailed to specifically elucidate this. The paraxial wave equation in cylindrical coordinates can be written as  $\nabla^2 U(z, r, \theta) \simeq (2ik\partial_z + \nabla_\perp^2)U(z, r, \theta) = 0$ , which

assumes that the function U evolves slowly in the propagation direction z. A solution using Laguerre-Gaussian modes can be written as

$$U(z, r, \theta) = \sum_{p,l} a_{p,l} F_{p,l}(X) \exp\left(il\theta + i\phi_{p,l} + iqX\right)$$
(1)

where  $X = r^2/w_{\rm b}^2(z)$  is a dimensionless radial coordinate,  $w_{\rm b}$  is the beam radius given by  $w_{\rm b}(z) = w_{\rm b,0}\sqrt{1+z^2/z_{\rm R}^2}$ , with  $w_{\rm b,0}$  being the width at focus, the Rayleigh length is  $z_{\rm R} = kw_{\rm b,0}^2/2$ , the Gouy phase is  $\phi_{p,l}(z) = -(2p+|l|+1)\arctan(z/z_{\rm R})$ ,  $a_{p,l}$  is a constant coefficient that informs of the mode amplitude, the factor  $q = z/2z_{\rm R}$  accounts for the wavefront curvature and  $F_{p,l}$  is given by the Laguerre-Gaussian function:

$$F_{p,l}(X) = \sqrt{\frac{p!}{(l+p)!}} X^{|l|/2} L_p^{|l|}(X) \exp(-X/2), \tag{2}$$

where  $L_p^{|l|}(X) = (p!)^{-1} \exp(X) X^{-1} d_X^p \left( \exp(-X) X^{(l+p)} \right)$  is a generalized Laguerre polynomial, as described by the Rodriguez representation, of degree p and l. The constant term in  $F_{p,l}$  is defined from the orthonormal condition  $\int_0^\infty dX F_{p,l}(X) F_{p',l}(X) = \delta_{p,p'}$ .

For a plane plasma wave, solution to the Poisson equation depends only on one coordinate z in the direction of wave propagation. By contrast, for twisted waves it is necessarily to consider a full three-dimensional solution to the Poisson equation that becomes

$$(2ik\partial_z + \nabla_\perp^2) \Phi = -e\epsilon_0^{-1} \delta n_e = -e\epsilon_0^{-1} \int d\mathbf{v} \delta f_e, \tag{3}$$

where -e is the electron charge,  $\Phi$  is the electric potential,  $\delta n_{\rm e}$  the perturbation to the electron density, and  $\delta f_{\rm e}$  the perturbation to the electron distribution function. The Poisson equation can be solved by considering  $\delta f_{e}$  written as sum of eigenmodes given by Laguerre-Gaussian functions. The set of solutions for the potential then becomes:

$$\Phi(z, r, \theta, t) = \sum_{p,l} \phi_{p,l} F_{p,l}(X) \exp(i\xi), \qquad (4)$$

and similarly for the perturbation to the electron distribution function:

$$\delta f_{e}(z, r, \theta, \mathbf{v}, t) = \sum_{p,l} f_{p,l}(\mathbf{v}) F_{p,l}(X) \exp(i\xi)$$
(5)

with the phase  $\xi = -\omega t + kz + l\theta + \psi_{p,l} + qX$ , where p is the radial mode number and l the azimuthal mode number.

To find the expression for the complex plasma wave frequency, including dispersion correction and Landau damping, we use the potential, given by the Poisson equation, and solve the linearized Vlasov equation for the electron distribution function in the paraxial approximation, which can be written as:

$$(-i\omega + ikv_z + \mathbf{v}_{\perp} \cdot \nabla_{\perp}) \, \delta f_{p,l} =$$

$$(-ikv_z - \mathbf{v}_{\perp} \cdot \nabla_{\perp}) \, e\Phi_{p,l} \partial_{\varepsilon} f_0,$$
(6)

where  $\partial_{\varepsilon} f_0$  is the derivative of the unperturbed electron distribution function  $f_0$  with respect to the electron kinetic energy  $\varepsilon$ . Since the unperturbed distribution function is assumed to be isotropic, only the electric field is retained in the linearized Vlasov equation. The case of plasma waves in a magnetized plasma<sup>23</sup> with an anisotropic electron distribution is out of the scope of this paper.

While the linearized paraxial Vlasov equation is already a simplification, solving it requires assessment of several issues. A particular problem occurs when considering the transverse gradient operator  $\mathbf{v}_{\perp} \cdot \nabla_{\perp}$ . This operator leads to the coupling of the neighboring plasma wave modes since the eigenfunctions to the paraxial Poisson equation are not eigenfunctions of the Vlasov equation. The physical implication is that the electron motion in the transverse directions couples the plasma wave modes.

This mode-coupling was ignored in the previous publication<sup>9</sup>, and an erroneous simplification was suggested by taking an average over of the transverse operator over a single mode. This inconsistent approach leads to incorrect expressions for the Landau damping rate and wave dispersion. Instead, we account for this mode-coupling effect by considering an expansion over the parameter  $1/kw_b \ll 1$ , being a small factor within the paraxial approximation.

The full derivation to the solution to the linearized Vlasov equation is described in Ref. 21. All of the operations carried out in the solution to Eq. (6) assume a small value for  $1/kw_b \ll 1$  and so only terms on the first order of this parameter are kept. The solution obtained gives the following expression for the longitudinal dielectric permittivity, which is valid within the Rayleigh length,  $|z| \lesssim z_R$ :

$$\epsilon(\omega, k) = 1 + \frac{e^2}{\epsilon_0 k^2} \times \int d\mathbf{v} \left[ \frac{\omega(\omega - kv_z)}{(\omega - kv_z)^2 - Nv_\perp^2 / w_b^2} - 1 \right] \partial_{\varepsilon} f_{e,0}, \tag{7}$$

where  $\omega$  is the plasma wave frequency, k the wavenumber and N=2p+|l|+1.

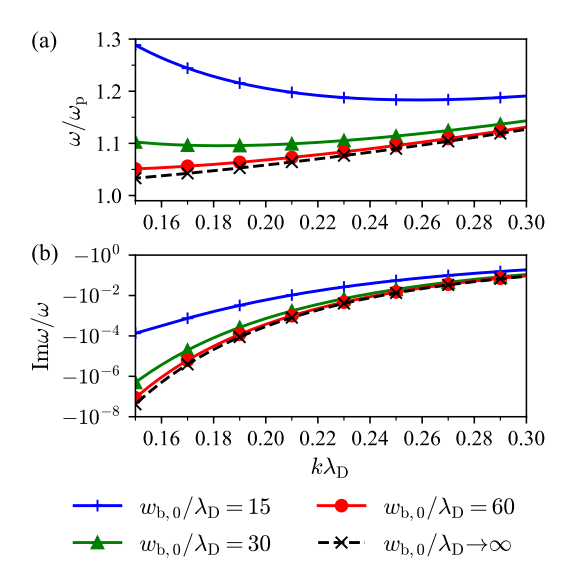


FIG. 1. Dispersion (a) and damping (b) of the helical plasma wave mode p = 0, l = 2 calculated from Eqs. (8) and (9) for the wave width shown in the legend. The black dashed line on panel (a) shows the Bohm-Gross dispersion corresponding to  $w_{\rm b,0}/\lambda_{\rm D} \to \infty$ , while the black dashed line on panel (b) shows the damping rate in the limit  $k^2\lambda_{\rm D}w_{\rm b,0} \gg 1$ .

The dispersion function  $\epsilon$  has a resonance, similar to the plane wave case, close to  $v_z = \omega/k$ . However this resonance is now split to  $v_z^{\pm} = \omega/k \pm (v_{\perp}/kw_b)\sqrt{N}$ . This widening of the resonance condition has interesting consequences which carry over into the non-linear Landau resonance regime and will be described in Section IV of this article. It is worth noting that the extra term in the resonance is non-zero even for a Gaussian beam as a consequence of the limited transverse dimension of the plasma wave.

For the case of a Maxwellian velocity distribution with a thermal velocity of  $v_{th}$ , using a Taylor expansion and assuming the limit  $k\lambda_{\rm D}\ll 1$ , one can find an explicit dispersion equation for helical plasma waves:

$$\frac{\text{Re}\,\omega_{\rm L}^2}{\omega_{\rm p}^2} = 1 + 3k^2\lambda_{\rm D}^2 + \frac{N}{k^2w_{\rm b}^2} \tag{8}$$

with the imaginary part giving the Landau damping rate:

$$\frac{\operatorname{Im}\omega_{L}}{\operatorname{Re}\omega_{L}} = -\sqrt{\frac{\pi}{8}} \frac{1}{k^{3}\lambda_{D}^{3}} \exp\left(-\frac{\omega^{2}}{2k^{2}v_{th}^{2}}\right) R\left(\frac{\sqrt{N/2}}{k^{2}\lambda_{D}w_{b}}\right),\tag{9}$$

where the function  $R(\zeta)$  is given by:

$$R(\zeta) = 1 + \sqrt{\frac{\pi}{2}} \zeta \exp\left(\frac{\zeta^2}{2}\right) \operatorname{erf}\left(\frac{\zeta}{\sqrt{2}}\right), \tag{10}$$

where  $\operatorname{erf}(x)$  denotes the error function with argument x,  $\lambda_{\mathrm{D}}$  is the Debye length, and  $\omega_{\mathrm{p}}$  is the electron plasma frequency.

These expressions self-consistently take into account the mode coupling that occurs when considering a three-dimensional plasma wave structure. The term arising from the beam-like structure of the plasma wave is proportional to  $1/k^2\lambda_D w_b$ . It is non-zero even for a Gaussian wave (l=0 mode) and it can be comparable or even dominate the thermal corrections. An example of the dispersion and damping rates of a helical wave and a comparison to the plane wave limit (where  $kw_b \to \infty$ ) is shown in Fig. 1.

# III. PLASMA WAVE STABILITY AND MAGNETIC FIELD GENERATION

In this section we describe the second order magnetic field associated with helical plasma waves. A selection of snapshots from the 3D PIC simulations are shown in Fig. 2. Figure 2(a,b) describes the l=1, l=2 helical plasma wave, whereas Fig. 2(c) presents results from the superposition of l=+2 and l=-2 plasma waves resulting in a standing helical plasma wave. Each panel of Fig. 2 shows the density displacement of each wave and a calculation of the magnetic field lines for each plasma wave are also shown. The axial magnetic field in the p=0, l=1 case appears weaker, and a significant amount of numerical noise can be seen in the plot. We first consider an analytical calculation of the magnetic fields, then we describe the set up of PIC simulations, and finally a comparison between the numerical simulations and the analytical theory is made.

#### Analytical calculation of helical plasma wave magnetic fields

While a paraxial helical plasma wave is electrostatic to first order on its amplitude, it can produce magnetic fields in the second order due to the finite radial extension of the plasma wave longitudinal electric field. As demonstrated by Bell and Gibbon<sup>25</sup>, a vector potential

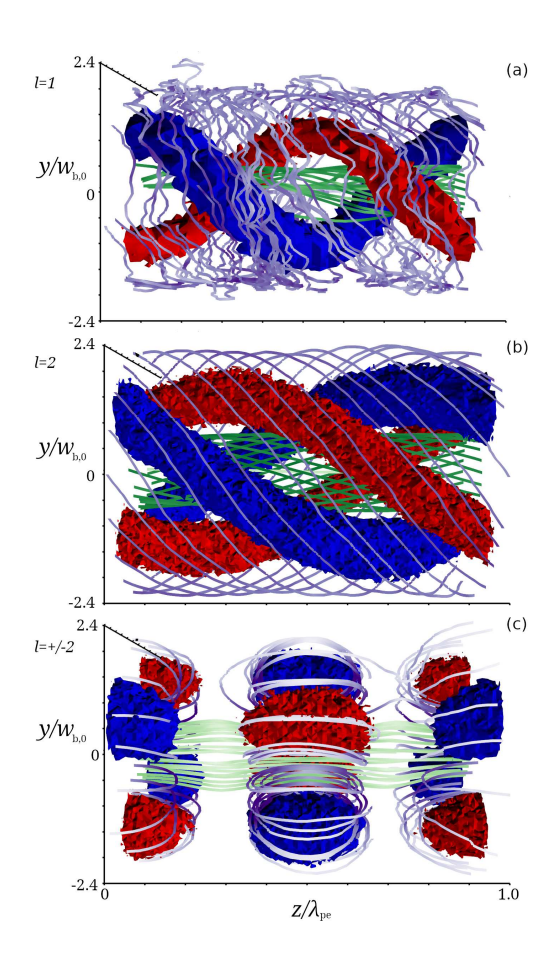


FIG. 2. Density perturbations and magnetic field lines in a twisted plasma wave obtained from simulations with the PIC code OCEAN<sup>24</sup>. Panel (a) shows a simulation of a traveling plasma wave mode p = 0, l = 1, (b) a traveling plasma wave mode p = 0, l = 2, (c) a standing wave mode p = 0,  $l = \pm 2$ . The surfaces of a constant density perturbation  $\delta n_{\rm e}/n_{\rm e,0}$  correspond to the positive (red) and negative (blue) perturbation at the level of 80% of the maximum density displacement. The magnetic field lines correspond to the interior (green) and exterior (purple) regions of the plasma wave. The magnetic field lines are calculated using the *Mayavi2* streamline package.

 $\mathbf{A}^{(2)}$  is associated with a second order oscillating current in a beam-like plasma wave:

$$(\partial_t^2 - c^2 \nabla^2 + \omega_p^2) \mathbf{A}^{(2)} = \epsilon_0^{-1} \mathbf{J}^{(2)}, \tag{11}$$

where  $\mathbf{J}^{(2)} = -\epsilon_0 (\delta n_e/n_{\mathrm{e},0}) \partial_t \mathbf{E}$  is the plasma wave current density, a product of the plasma wave electric field  $\mathbf{E}$  and density perturbation  $\delta n_e/n_{\mathrm{e},0}$ , both of them proportional to the plasma wave potential  $\Phi_{p,l}$ . A magnetic field can then be calculated from this vector potential using the relation  $\mathbf{B}^{(2)} = \nabla \times \mathbf{A}^{(2)}$ . For a single mode plasma wave near the focal region  $(w_b \simeq w_{b,0})$  the magnetic field is static in time and has two components in the axial  $\mathbf{e}_z$  and

azimuthal  $\mathbf{e}_{\theta}$  directions:

$$\mathbf{B}^{(2)} = \frac{keE_0^2}{m_e\omega_p^3w_b} \left(F_{p,l}^2(X)\right)' \left[\mathbf{e}_\theta\sqrt{X} - \mathbf{e}_z \frac{l}{kw_b}\right],\tag{12}$$

where  $m_e$  is the electron mass and  $E_0$  is the plasma wave electric field amplitude. Full details for the calculation of the magnetic field can be found in Ref. 10. The same method can be applied to obtain a field for the helical standing plasma wave. In this case the magnetic field has non-zero axial and radial components,  $B_z$  and  $B_r$ :

$$\mathbf{B}^{(2)} = \frac{lkeE_0^2}{2m_e\omega_p^3 w_b} \left[ \mathbf{e}_z \frac{\left(F_{p,l}^2(X)\right)'}{kw_b} \left( 1 + \frac{\omega_p^2 \cos(2kz)}{4k^2c^2 + \omega_p^2} \right) - \mathbf{e}_r \frac{F_{p,l}^2(X)}{\sqrt{X}} \frac{\omega_p^2 \sin(2kz)}{4k^2c^2 + \omega_p^2} \right].$$
(13)

While static in time, magnetic field oscillates along the propagation axis with a wavenumber double that of the electric field oscillation. The derivation of this formula is given in Appendix A.

It is worth noting that the magnetic field obeys the zero divergence condition:  $\nabla \cdot \mathbf{B}^{(2)} = 0$ , which in the case of traveling wave reads:  $\partial_z B_z + r^{-1} \partial_\theta B_\theta = 0$ , and in the case of the standing wave:  $\partial_z B_z + \partial_r B_r = 0$ . The structure and magnitude of the magnetic fields is verified in the PIC calculation for the p = 0, l = 2 mode where the magnetic fields are seen to be static with only minor fluctuations in the amplitude. A snapshot in time of the PIC results compared to the magnetic field calculations described by Eq. (12) can be seen in Fig. 3.

The second order magnetic field is not necessarily weak in experiments. A plasma wave of a wavelength of 400 nm, width of 8 µm ( $kw_0 = 40\pi$ ) and amplitude  $a_0 = eE_0/m_ec\omega_p = 0.2$  excited in a plasma of density  $n_e = 1.7 \times 10^{19}$  cm<sup>-3</sup> will generate a magnetic field of approximately 4 T (or 40 kG) in the azimuthal direction. This magnetic field depends on the plasma wave radius as  $B \propto (a_0/kw_b)^2$ , which may enable the generation of significantly higher magnetic fields for smaller values of  $kw_b$  or larger wave amplitudes.

# 3D PIC simulations of helical plasma wave magnetic fields

The stability of helical plasma waves is tested in numerical simulations with the PIC code OCEAN<sup>24</sup>. The representative simulations showing the excitation of three different plasma wave modes are discussed below. In two simulations we excite traveling waves with mode

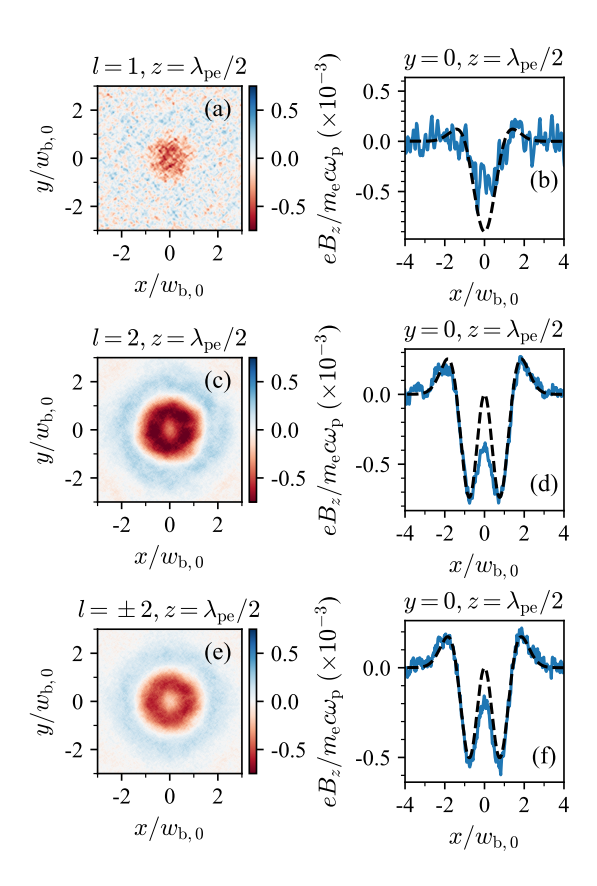


FIG. 3. Transverse slices (a), (c), and (e) and line-outs from those slices (b), (d) and (f) of the magnetic field  $B_z$  generated by helical plasma waves in three PIC simulations. The locations of slices and line-outs are described above each plot. Panels (a) and (b) correspond to a traveling helical plasma wave mode p = 0, l = 1 (see Fig. 2(a)). Panels (c) and (d) correspond to a traveling plasma wave mode p = 0, l = 2 (see Fig. 2(b)). Panels (e) and (f) correspond to a standing plasma wave mode p = 0,  $l = \pm 2$  (see Fig. 2(c)). The black dashed lines show theoretical predictions of  $B_z$  for each mode according to Eq. (12) for panels (b) and (d) using amplitudes  $a_0 = 0.15$  and  $a_0 = 0.2$  respectively, and Eq. (13) for panel (f), using a mode amplitude of  $a_0 = 0.22$ . The data is plotted after a 3D Gaussian filter with a width of 1 cell used to remove high frequencies.

indices p = 0, l = 1 and p = 0, l = 2. In the third simulation we excite a standing wave mode with p = 0 and l = 2, which is equivalent to a pair of counter-propagating p = 0 modes with  $l = \pm 2$  so the azimuthal component of the current is present. A detailed description of the simulation of the p = 0, l = 2 mode can be found in Ref. 10. For completeness the full details for the three simulations, along with the procedure used to excite the plasma wave, are described in Appendix B.

To ensure that the excited plasma wave is stable, the plasma temperature and density are chosen such that there is no Landau damping within the simulation. This was done by choosing a relatively low plasma temperature,  $T_{\rm e} = 1.54 \times 10^{-3} m_{\rm e} c^2$  and setting a large plasma wave phase velocity,  $v_{ph} = \omega/k = c$ . The plasma wave width  $w_{\rm b} = 5 \ c/\omega_{\rm p}$  is chosen such that the paraxial approximation is verified,  $1/kw_{\rm b} = 0.2$ , and coupling to other modes in Eq. (9) is minimized,  $1/k^2w_{\rm b}\lambda_{\rm D} = 0.2$ . To avoid exciting ion acoustic waves, fixed ions are considered.

The length of the box is chosen to exactly fit one wavelength with  $kL_z = 2\pi$ . The box is filled with a fully ionized uniform hydrogen plasma with the cell side length equal to one Debye length  $\Delta l = \lambda_{\rm D}$ . In order to observe the second order magnetic field, the signal-to-noise is kept at a sufficiently low level by using 100 macro-particles per cell per species. The transverse boundary conditions are chosen to be absorbing for both particles and fields. This choice is motivated by the fact that orbital angular momentum is extrinsic and so any interaction from nearby plasma waves, via periodic boundary conditions in the transverse directions could complicate the wave dynamics.

The wave is excited over 10 plasma periods,  $T_p = 2\pi/\omega_p$ , by using a weak driving force  $\mathbf{E}_{\rm d}$  calculated from  $\mathbf{E}_{\rm d} = -\nabla\Phi_{p,l}$ . Details regarding the excitation process are discussed in Ref. 22 and in Appendix B. After the initial excitation time  $t = 10T_p$ , the driving force  $\mathbf{E}_{\rm d}$  removed, and the plasma wave is allowed to oscillate freely. An amplitude of  $0.15 < a_0 < 0.25$  is achieved for each plasma wave, which is smaller than the driver amplitude due to slight frequency mismatching of  $\mathbf{E}_{\rm d}$  with the excited plasma wave, and slight absorption at the otherwise periodic axial boundaries. Figure 2 shows three-dimensional renderings of the plasma wave density perturbation and magnetic field lines for the resulting plasma waves at a time  $t = 14T_{pe}$  after the driving field  $\mathbf{E}_{\rm d}$  is removed.

Selected results from the particle-in-cell simulations can be seen in Figs. 3 and 4 where the non-zero components of the second order magnetic field is plotted. The remaining magnetic field components ( $B_r$  in the case for traveling waves, and  $B_\theta$  in the case for the standing wave) are at the noise level. The axial component of magnetic field  $B_z$  is plotted in Fig. 3 at a time of  $14T_p$  after the driving field  $\mathbf{E}_d$  is removed. The simulation for p=0, l=2 standing and traveling waves are run for a total time of  $20T_p$  after the driver is removed and show stable magnetic fields until the end of the simulations. The PIC results for the axial magnetic field match the analytical formulas to a high degree. The axial magnetic field is

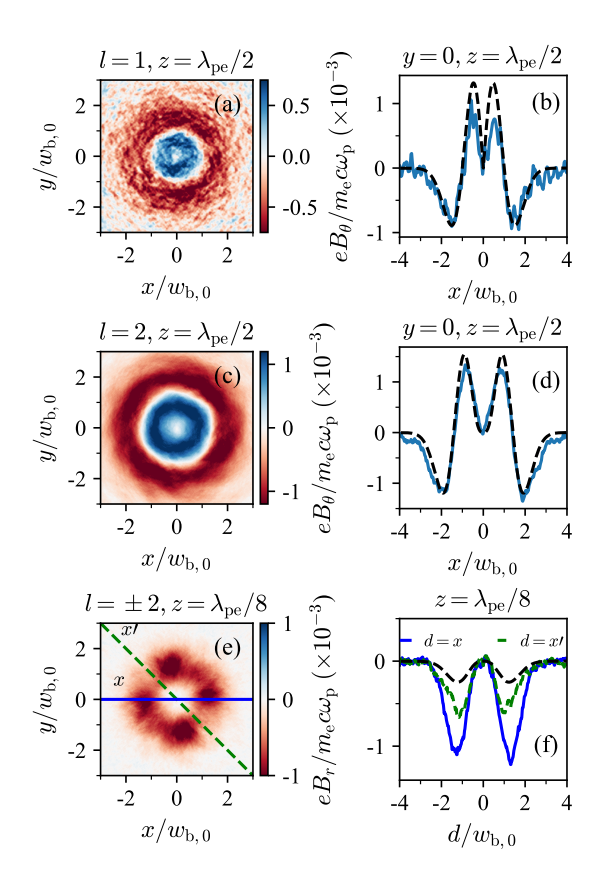


FIG. 4. Transverse slices (a), (c), and (e) and line-outs from those slices (b), (d) and (f) of the non-zero transverse components of the magnetic field generated by helical plasma waves in three PIC simulations. The locations of slices and line-outs are described above each plot. Panels (a) and (b) show the azimuthal magnetic field  $B_{\theta}$  generated by a traveling helical plasma wave mode p = 0, l = 1 (see Fig. 2(a)). Panels (c) and (d) show the azimuthal magnetic field  $B_{\theta}$  for a traveling plasma wave mode p = 0, l = 2. Panels (e) and (f) show the radial magnetic field  $B_r$  for a standing plasma wave mode  $p = 0, l = \pm 2$ . Two line-outs shown in panel (f) correspond to the cuts shown in panel (e) using the matching line styles. The black dashed lines show theoretical predictions of  $B_{\theta}$  for each mode according to Eq. (12) for panels (b) and (d) using amplitudes  $a_0 = 0.15$  and  $a_0 = 0.2$  respectively, and Eq. (13) for panel (f) using a mode amplitude of  $a_0 = 0.22$ 

uniquely from the helical structure of the electric field.

The PIC simulation results for the non-zero transverse magnetic field components ( $B_r$  in the standing case, and  $B_{\theta}$  in the traveling case) are shown in Fig. 4. The traveling waves, both l = 1 and l = 2, have azimuthal transverse magnetic field  $B_{\theta}$  that shows a good match to the analytical predictions. The lower signal to noise ratio observable in the

l=1 simulation is due to both a weaker coupling between the driving electric field and excited plasma wave, and additional numerical noise. Both of these effects are due to the lower resolution used for this simulation (see Table I). The PIC results for the standing wave, however, show several discrepancies when compared to the analytical calculation (see Fig. 4(e) and (f)). The most obvious one is the magnitude of  $B_r$ , which is two times larger compared to the theoretical prediction. The second discrepancy is that there is an oscillation in the azimuthal direction seen in the numerical calculations which is not expected in the theory. The frequency of this oscillation is  $2\omega_p$ , so it is possible that it is related to the insufficient resolution of the PIC code in the longitudinal direction.

The larger  $B_r$  field may also be explained by a mismatched driving field leading to excitation of additional small-amplitude non-resonant modes. The description of the magnetic fields described by Eq. (13) requires that the time-varying terms in the second order vector potential  $\mathbf{A}^{(2)}$  (calculated in Appendix A) exactly cancel when calculating  $\nabla \times \mathbf{A}^{(2)} = \mathbf{B}^{(2)}$ . A frequency mismatch may change the contribution of the axial and azimuthal currents to the radial magnetic field  $B_r$ , which would have both a static component and a component that oscillates in time at a frequency of  $2\omega_p$ .

# IV. TRANSFER OF ORBITAL ANGULAR MOMENTUM TO ELECTRONS

In this section the motion of resonant electrons within a helical plasma wave is considered. Analytical expressions for the electron trajectories are illustrated with numerical calculations for different initial conditions.

## Electron motion in a helical plasma wave

Electron dynamics is obtained from the non-relativistic equations of motion:

$$d_t \mathbf{r}_{\mathrm{e}} = \mathbf{v}_{\mathrm{e}}$$
 and  $m_{\mathrm{e}} d_t \mathbf{v}_{\mathrm{e}} = -e \mathbf{E}$ 

with the electric field of plasma wave calculated from the potential Eq. (4). For a single traveling plasma wave mode an electric field reads:

$$E_z = E_0 F_{p,l}(X) \sin(kz - \omega t + l\theta), \tag{14}$$

$$E_{\theta} = \frac{lE_0}{kw_b} X^{-1/2} F_{p,l}(X) \sin(kz - \omega t + l\theta), \tag{15}$$

$$E_r = -\frac{2E_0}{kw_b} X^{1/2} F'_{p,l}(X) \cos(kz - \omega t + l\theta).$$
 (16)

According to Eqs. (14) and (15), the electron momentum increments in the axial and azimuthal directions are related as  $\Delta p_z/\Delta p_\theta = kr/l$ . This leads to the relationship between the axial momentum  $p_z$  and orbital axial momentum  $l_z = rp_\theta$ :

$$l\Delta p_z = kl_z + Am_e c, (17)$$

where A is an integration constant depending on initial conditions. The radial momentum  $\Delta p_r$ , however, is out of phase with  $\Delta p_z$  and  $\Delta l_z$ .

The Beeman integration routine<sup>26</sup> is used in numerical calculation of electron trajectories, due to it's simplicity of implementation. A small amplitude,  $eE_0/m_e\omega v_{ph}=10^{-4}$ , plasma wave mode  $p=0,\ l=1$  is considered, so the second order effects can be neglected. Two representative initial conditions correspond either to a non-resonant electron initially at rest,  $\mathbf{v}_0=0$ , or to a resonant electron traveling close to the plasma wave phase velocity,  $v_{z,0}=0.99v_{ph}$  and  $v_{y,x,0}=0$ . The relative strength of the electric field in a plasma wave vary with radial position r and so initial positions in the range  $r_0/w_b=0.1 \rightarrow 2.0$  are considered. The electrons are tracked within the focal region of the plasma wave,  $|z| < z_{\rm R}$ . The motion of electrons is followed over time interval of  $25T_p$ . The electron trajectories and phase plots are shown in Fig. 5.

Non-resonant electrons perform an oscillatory movement with the radial velocity  $v_r$  phaseshifted by a quarter of period with respect to  $v_z$  and  $v_\theta$  (see Fig. 5(a) and (c)). Thus, there is no net transfer of momentum from the wave to the non-resonant particles. This is expected given that the corresponding components of electric field, Eqs. (14), (15) and (16), have similar phase differences. The velocities  $v_z$  and  $v_\theta$  oscillate in phase, which is described by a straight line in Fig. 5(e) in agreement with Eq. (17). The size and shape of the electron's orbits in phase space vary as a function of r. The radial oscillation swaps direction at  $r = 1.5w_0$  due to the reversal in the sign of the radial electric field  $E_r$ , seen in Fig. 5(g).

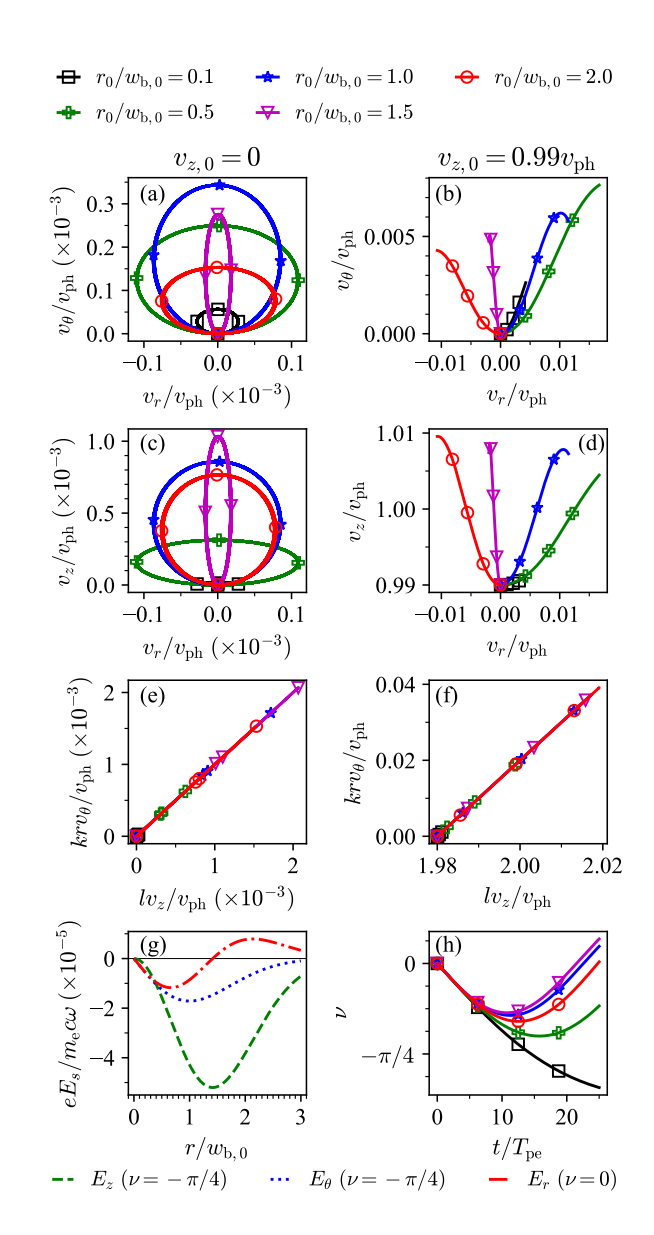


FIG. 5. Trajectories and phase plots of test electrons initiated at  $\theta_0 = \pi/2$  and several radial positions  $r_0$  indicated in the figure. Panels (a), (c), and (e) show the velocity of a non-resonant electron with varying initial radial position  $r_0$ ,  $v_{z,0} = 0$ , and initial phase  $\nu = 0$ , over 25 plasma periods. Panels (b), (d), and (f) show the velocity of a resonant electron with the same initial conditions except  $v_{z,0} = 0.99v_{ph}$ , over the same time. Panel (g) shows the radial profile of the electric field with a phase of  $\nu = 0$  for  $E_r$ , and  $\nu = -\pi/4$  for  $E_z$  and  $E_\theta$ . Panel (h) shows the phase  $\nu$  of the plasma wave electric field experienced by the resonant particles over time. The phase of the field is found from  $\nu = kz - \omega t + l\theta$ .

This change in sign of the radial velocity corresponds to the change in sign of the magnetic

field in Fig. 3.

A markedly different behavior is observed for resonant electrons with velocity close to the phase velocity, see Fig. 5(b), (d), (f) and for the phase of the electric field experienced by the electrons (h). Each electron experiences a slowly varying local electric field, which results in a regular change of the momentum with time, both in axial and transverse directions. While a linear relationship between the axial and azimuthal velocities,  $v_z$  and  $v_\theta$ , in Fig. 5(g) is similar to the non-resonant electrons, their values are one order of magnitude larger. The deviation from the linear relationship occurs due to changes of electron radial position over time, which alters the ratio between  $E_z$  and  $E_\theta$  in a non-linear fashion.

The trajectories of electrons vary significantly as a function of the initial radial position. The inner electrons with  $r_0 \lesssim 1.5w_0$  are accelerated outwards, while the outer electrons are accelerated inwards. This results in the bunching of resonant electrons at the position  $r_0 \sim 1.5w_0$ , corresponding to the zero of the radial electric field, and a significant non-zero net transfer of momentum and energy over the time of  $25T_p$  from the wave to the resonant particles. This behavior is similar to that observed when helical light interacts with electrons<sup>27</sup>, the impact of which requires further study.

#### V. NON-LINEAR DAMPING OF HELICAL PLASMA WAVES

This section presents a brief overview of results related to the energy and momentum exchange of a helical plasma wave with electrons in the nonlinear regime. The previous work<sup>22</sup> described the helical plasma wave damping in the kinetic regime  $k\lambda_D > 0.3^{20}$  due to the trapping of resonant electrons in the wave. In contrast with the linear regime, where the Landau damping coefficient given by Eq. (9) is calculated from the unperturbed electron distribution function, the simulations presented in Ref. 22 correspond to the case where the helical plasma wave strongly modifies the electron distribution in the phase space.

Four simulations detailed in Ref. 22 present the dynamics of resonant electrons in a Gaussian wave mode p = 0, l = 0, and three Laguerre-Gaussian modes l = 1, 2 and 4. The same method of gradual excitation as described in Appendix B is used, however, the plasma temperature was higher,  $T_{\rm e} = 0.03 m_{\rm e} c^2$ , such that  $k\lambda_{\rm D} = 0.33$  and a significant number of electrons may resonantly interact with the wave. The frequency of each plasma wave was measured at several positions along the z-axis and at the radial positions of the axial electric

field maximum. It is observed that the frequency of helical plasma wave decreases as its amplitude increases. This is explained by the particle trapping inline with the kinetic theory of plane plasma waves<sup>28–30</sup>. The frequency measured was the same,  $\omega = 1.11 \pm 0.01 \omega_{\rm p}$ , for the all four considered cases.

Particle trapping is observed by plotting the electron motion in phase space. In a plane or Gaussian plasma wave the electrons with velocity close to the phase velocity perform a rotation in the phase space z,  $p_z$  alternating between accelerating and decelerating phases of the plasma wave electric field. For a helical plasma wave the phase-space rotation occurs in a twisted phase space described by  $\tilde{z}$ ,  $p_z$ , where  $\tilde{z} = z + l\theta/k$  where the accelerating/decelerating phases are twisted about the z-axis l times per wavelength.

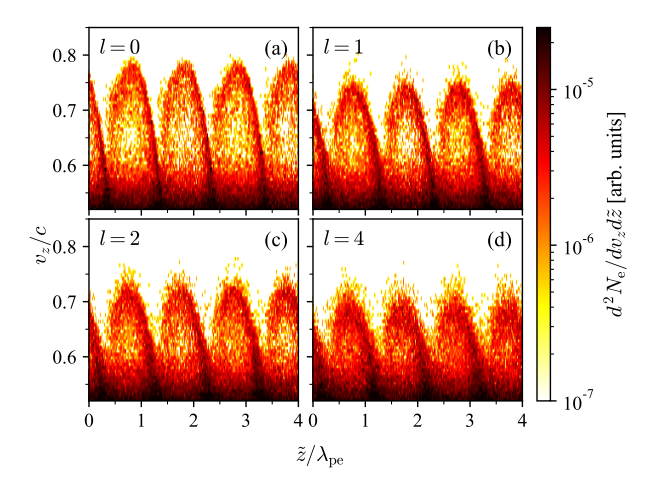


FIG. 6. Distribution of electrons in the phase space,  $\tilde{z}$ ,  $v_z$  averaged over the transverse coordinate r and transverse velocities  $v_r$  and  $v_\theta$ . Here  $\tilde{z} = z + l\theta/k$ ,  $\lambda_{pe} = 2\pi/k$  and  $v_{ph} = 0.615c$ . A Gaussian mode p = 0, l = 0 (a), and three Laguerre-Gaussian modes with p = 0, and l = 1 (b), 2 (c) and 4(d) are considered. The results are presented at a time  $t = 9.5 T_p$ .

Figure 6 shows the phase plot in the plane  $\tilde{z}, p_z$  where the resonant particles are trapped and oscillate around the phase velocity  $v_{ph} = 0.615c$ . The distribution function, which is retrieved from numerical simulation at time  $9.5T_p$ , is integrated over the transverse velocities  $v_r$  and  $v_\theta$  and in the transverse plane  $r, \theta$ . In order to account for azimuthal displacement of trapped particles in the helical wave, integral over the azimuthal angle is performed in the tilted plane,  $\theta, z - l\theta/k$ , while keeping constant the tilted coordinate  $\tilde{z} = z + l\theta/k$ .

The amplitude of electron oscillations decreases with the orbital number l, but a difference between the Landau damping rate across modes in such a nonlinear regime is difficult to

quantify as the simulation comprises several bounce periods. The damping is suppressed due to the rapid phase mixing and formation of a plateau in the distribution function close to the phase velocity of the plasma waves. Once the plateau is formed, there is a roughly equal quantity of trapped electrons traveling above and below the phase velocity, resulting in a zero net energy exchange between the particles and the wave.

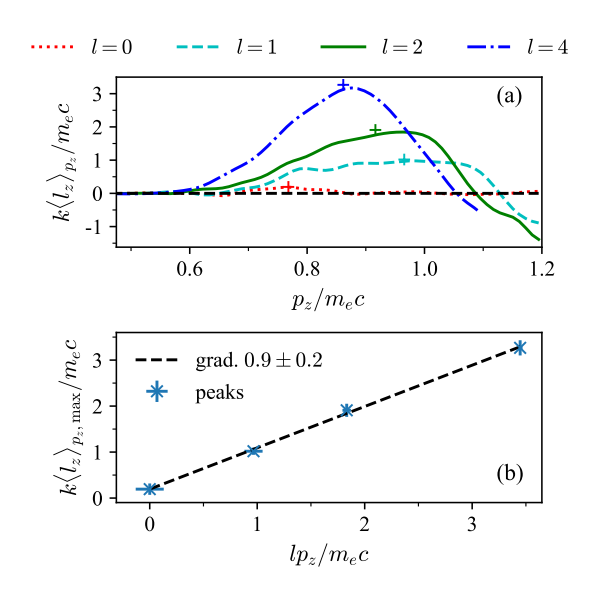


FIG. 7. Correlation between the axial momentum  $p_z$  and OAM  $\langle l_z \rangle_{p_z}$  averaged over the perpendicular components of the electron momentum and radial coordinate. Panel (a) shows  $k \langle l_z \rangle_{p_z}$  as a function of  $p_z$  separately for each mode. The + markers show the maximum value calculated from a Gaussian fit. Panel (b) shows dependence of this maximum value,  $k \langle l_z \rangle_{p_z,\text{max}}$  on  $lp_z$ , where l is the azimuthal mode number. The gradient of the fitted straight line is  $0.9 \pm 0.2$  with intercept  $A = 0.04 \pm 0.05$  is in good agreement with Eq. (17). Reprinted figure with permission from [D. R. Blackman, R. Nuter, P. Korneev, and V. T. Tikhonchuk, Phys. Rev. E 102, 033208 (2020).] Copywrite (2020) by the American Physical Society.

The correlation between the gain of OAM and axial momentum resonant electrons predicted by Eq. (17) is verified in Fig. 7. In panel (a) we show  $l_z$  for a given  $p_z$  averaged over the perpendicular components of the electron momentum and radial coordinate,  $\langle l_z \rangle_{p_z}$ . The gain is observed for the axial electron velocities  $v_z$  above the minimum velocity  $v_{\min} \simeq 0.5c$ , which is slightly below the phase velocity  $v_{ph} = 0.615c$ . The maximum gain of OAM increases with l, but the corresponding axial momentum  $p_{z,\max}$  decreases. This relation is further exploited in Fig. 7(b), where the maximum value of OAM,  $k\langle l_z \rangle_{p_z,\max}$  as a function

of the axial momentum  $lp_{z,\text{max}}$  corresponding to the position of this maximum. A linear relation between the OAM gain the characteristic axial momentum is indeed in good agreement with the theoretical prediction given by Eq. (17).

A detailed study of the OAM transfer from the plasma wave to resonant particles in the linear regime is presented in Ref. 21. It is demonstrated analytically that energy, axial momentum, and OAM are dissipated from the plasma wave at the same rate. Inline with the numerical calculations presented in Section IV, the radial velocity of electrons within the plasma wave does not affect the OAM transfer between wave and particle. In the linear regime the total rate of transfer of OAM from wave to particles can be written as:

$$\frac{1}{\mathcal{L}_z} \frac{d\mathcal{L}_z}{dt} = \frac{e^2 \omega^2}{\epsilon_0 k^2} \int d\mathbf{v} \frac{\partial_{\epsilon} f_{e,0}}{\sqrt{(v_\perp l/r)^2 - (kv_z - \omega)^2}},\tag{18}$$

where  $\mathcal{L}_z$  is the local value of the OAM  $l_z$  averaged over the electron distribution function and the plasma wave period. As can be seen from the denominator in the right hand side of this expression, resonant particles make a dominant contribution. In the case of a Maxwellian distribution the rate of OAM transfer reads:

$$\frac{1}{\mathcal{L}_z} \frac{d\mathcal{L}_z}{dt} = \sqrt{\frac{\pi}{8}} \frac{\omega}{k^3 \lambda_D^3} \exp\left(-\frac{\omega^2}{2k^2 v_{th}^2} + \frac{l^2}{2k^2 \lambda_D r}\right). \tag{19}$$

The above expression shows important dependence of the dissipation rate on the radial coordinate. Near the plasma wave axis, where  $k^2\lambda_{\rm D}r\lesssim l^2$ , the transfer of plasma wave OAM to resonant particles is increased over the Landau damping rate described by Eq. (9). For the helical plasma waves described in Ref. 10 this limit is reached (noting that  $k\lambda_{\rm D}\simeq 0.3$  and  $kw_{\rm b}=6$ ) for radial positions where  $r\lesssim 0.6w_{\rm b}l^2$ . The role of this effect in the non-linear Landau damping regime remains to be investigated.

### VI. DISCUSSION

This article provides a brief overview of the research carried out in Refs. 10, 21, and 22 along with several new results of simulations of plasma wave magnetic fields and particle trajectories within a plasma wave.

A self-consistent solution for the Landau damping of helical plasma waves in the linear regime<sup>10</sup> takes into account in the paraxial approximation the coupling between Laguerre-Gaussian modes in a helical plasma wave. This results in the modification of the wave dispersion and damping.

The 3D PIC simulations show the stability of helical plasma wave structure and complex magnetic field structures associated with the rotational component of the plasma wave ponderomotive force. The unique longitudinal magnetic field structure seen with plasma waves with OAM matches the analytical predictions well in both structure and magnitude for small amplitude plasma waves. The manuscript presents new results demonstrating the magnetic field structure of a standing plasma wave with OAM, which is investigated both analytically and in a PIC simulation. The standing wave shows a strong longitudinal component along with a radial component sensitive to small deviations from the analytical result. These magnetic fields should be observable in a laboratory by using high power lasers for driving helical plasma waves in low density gas jets.

For electrons traveling close to the phase velocity of the plasma wave a clear relationship between the exchange of longitudinal momentum and OAM is demonstrated in both analytical and numerical calculations. The trapped resonant electrons acquire a significant OAM which is proportional to the gain of the axial momentum. A novel result from the analysis performed in Section V shows that the transverse fields play a role not only in the transfer of OAM from wave to particle but in constraining electrons to the regions of the plasma wave where the electric field is strongest. Other processes of wave-particle interactions in high energy density (HED) plasmas involving the OAM transfer are yet to be explored. These phenomena include three wave interactions, such as stimulated Raman scattering, may be strongly affected by the OAM kinetics<sup>31–34</sup>. Interesting results are likely to be yielded from an investigation into OAM plasma wave dynamics in more complex HED plasma physics scenarios.

## VII. ACKNOWLEDGMENTS

This research was supported by the National Science Foundation (Grant No. 1903098). This work used the Extreme Science and Engineering Discovery Environment (XSEDE), which is supported by National Science Foundation grant number ACI-1548562. The XSEDE resource Stampede2, under allocation TG-PHY190034, was used for performing a 3D kinetic particle-in-cell simulation in support of results seen in this manuscript. This work was granted access to HPC resources of TGCC under the allocation A0010506129 made by GENCI. We acknowledge PRACE for awarding us access to resource Joliot Curie-SKL based

in France at TGCC Center. The work was partially supported by the Foundation for the Advancement of Theoretical Physics and Mathematics "BASIS".

# Appendix A: Standing plasma wave magnetic field calculation

A helical plasma wave can be constructed from two plasma waves with opposing helicities and phase velocities, but with otherwise identical mode structure. Interference of such two modes generates a plasma wave with only rotational motion in the phase. To calculate the magnetic field of the standing helical plasma wave the lowest moments of the electric current and electron density can be found using the Poisson and Ampere equations. The following derivation assumes that the dispersion can be neglected ( $\omega \simeq \omega_p$ ), and that  $|z| < z_R$ . The potential of a twisted standing plasma wave is given by:

$$\phi = 2\phi_{p,l}F_{p,l}(X)\cos(kz)\cos(\omega t - l\theta). \tag{A1}$$

The electric field can then be found from the relation  $\mathbf{E} = -\nabla \phi$ :

$$E_z = E_0 F_{p,l}(X) \sin(kz) \cos(\omega t - l\theta), \tag{A2}$$

$$E_{\theta} = \frac{lE_0}{kw_b} \frac{F_{p,l}(X)}{\sqrt{X}} \cos(kz) \sin(\omega t - l\theta), \tag{A3}$$

$$E_r = -\frac{2E_0}{kw_b} \sqrt{X} F'_{p,l}(X) \cos(kz) \cos(\omega t - l\theta)$$
(A4)

where  $E_0 = 2k\phi_{p,l}$ . The electron density is calculated from the paraxial version of the Poisson equation<sup>10</sup>:  $k^2\phi = e\epsilon_0^{-1}\delta n_e$ , which gives

$$\frac{\delta n_{\rm e}}{n_{\rm e,0}} = -\frac{keE_0}{m_{\rm e}\omega_{\rm p}^2} F_{p,l}(X) \cos(kz) \cos(\omega t - l\theta). \tag{A5}$$

The electric currents, given by  $\mathbf{j} = -\epsilon_0 \partial_t \mathbf{E}$  are:

$$j_z = \epsilon_0 \omega E_0 F_{p,l}(X) \sin(kz) \sin(\omega t - l\theta), \tag{A6}$$

$$j_{\theta} = -\frac{\epsilon_0 \omega l E_0}{k w_b} \frac{F_{p,l}(X)}{\sqrt{X}} \cos(kz) \cos(\omega t - l\theta), \tag{A7}$$

$$j_r = -\frac{2\epsilon_0 \omega E_0}{k w_b} \frac{F'_{p,l}(X)}{\sqrt{X}} \cos(kz) \sin(\omega t - l\theta). \tag{A8}$$

Using trigonometric identities to simplify the second order terms, the current density  $\mathbf{J}^{(2)} =$ 

 $\mathbf{j}\delta n_{\mathrm{e}}/n_{\mathrm{e},0}$  reads:

$$J_{z}^{(2)} = -\frac{ke\epsilon_{0}E_{0}^{2}}{4m_{e}\omega_{p}}F_{p,l}^{2}(X)\sin(2kz)\sin(2(\omega t - l\theta)),$$

$$J_{\theta}^{(2)} = \frac{e\epsilon_{0}lE_{0}^{2}}{4m_{e}\omega_{p}kw_{b}}\frac{F_{p,l}^{2}(X)}{\sqrt{X}}\left[1 + \cos(2kz) + \frac{1}{2}(k^{2}+k^{2})\right]$$
(A9)

$$\cos(2kz)\cos(2(\omega t - l\theta)) + \cos(2(\omega t - l\theta)) \, , \tag{A10}$$

$$J_r^{(2)} = -\frac{2e\epsilon_0 E_0}{4m_e \omega_p k w_b} \frac{F_{p,l}(X) F'_{p,l}(X)}{\sqrt{X}} \times \sin(2kz) \left[1 + \cos(2(\omega t - l\theta))\right]. \tag{A11}$$

The second order vector potential given by Eq. (11) components:

$$A_z^{(2)} = -\frac{keE_0^2}{4m_e\omega_p}F_{p,l}^2(X)\frac{\sin(2kz)\sin(2(\omega t - l\theta))}{(4k^2c^2 - 3\omega_p^2)},$$
(A12)

$$A_{\theta}^{(2)} = \frac{elE_0^2}{4m_{\rm e}\omega_{\rm p}kw_{\rm b}} \frac{F_{p,l}^2(X)}{\sqrt{X}} \Bigg[ \frac{1}{\omega_{\rm p}^2} + \frac{\cos(2kz)}{(4k^2c^2 + \omega_{\rm p}^2)} +$$

$$\frac{\cos(2kz)\cos(2(\omega t - l\theta))}{(4k^2c^2 - 3\omega_p^2)} + \frac{\cos(2(\omega t + l\theta))}{3\omega_p^2} \bigg],\tag{A13}$$

$$A_r^{(2)} = -\frac{2eE_0}{4m_e\omega_p kw_b} \frac{F_{p,l}(X)F'_{p,l}(X)}{\sqrt{X}} \times$$

$$\frac{\sin(2kz)}{(4k^2c^2 + \omega_{\rm p}^2)} \left[ \frac{1}{\omega_{\rm p}^2} - \frac{\cos(2(\omega t - l\theta))}{3\omega_{\rm p}^2} \right]. \tag{A14}$$

The second order magnetic field can then be calculated from the vector potential  $\nabla \times \mathbf{A}^{(2)} = \mathbf{B}^{(2)}$ :

$$B_z^{(2)} = \frac{2elE_0^2}{4m_e\omega_p w_b^2} \left(F_{p,l}^2\right)' \left[\frac{1}{\omega_p^2} + \frac{\cos(2kz)}{4k^2c^2 + \omega_p^2}\right],\tag{A15}$$

$$B_{\theta}^{(2)} = 0,$$
 (A16)

$$B_r^{(2)} = -\frac{2kelE_0^2}{4m_e\omega_p w_p} \frac{F_{p,l}^2}{\sqrt{X}} \frac{\sin(2kz)}{(4k^2c^2 + \omega_p^2)}.$$
 (A17)

## Appendix B: Particle in Cell Simulation Details

The simulations parameters used to generate the results seen in Figs. 2, 3 and 4 are detailed in Table I. To generate the plasma waves, a small amplitude field is introduced into

## Simulation parameters:

Plasma Simulation	Standing/	Traveling $l = 1$
	Traveling $l=2$	
Transverse size (cells)	$1200 \times 1200$	$1000 \times 1000$
Longitudinal size (cells)	160	80
Transverse B.C.	absorbing	absorbing
Longitudinal B.C.	periodic	periodic
Cell side length	$0.0125\pi \ c/\omega_{\mathrm{p}}$	$0.025\pi \ c/\omega_{\rm p}$
Time step	$T_p/160$	$T_{p}/80$
Electron temperature	$1.5 \times 10^{-3} m_{\rm e} c^2$	$7 \times 10^{-3} m_{\rm e} c^2$
Macro-particles	100	100
(per cell per species)		
Ion species	Fixed $H^+$	Fixed $H^+$

TABLE I. 3D PIC simulations parameters used for calculations of magnetic fields. The plasma waves were excited with a box of a length  $L_z$  equal to the plasma wavelength  $\lambda_{pe} = 2\pi/k$ . A width parameter  $w_b = 5 c/\omega_p$ . The electron density  $n_e$  is fixed by selecting the appropriate value of  $\omega_p$ .

the plasma in order to generate a perturbation in the plasma wave of the desired type. The plasma wave and obeys an equation of a driven oscillator:

$$\partial_t^2 \mathbf{E}_{pe} + \omega_{\mathcal{L}}^2 \mathbf{E}_{pe} = \omega^2 \mathbf{E}_d \tag{B1}$$

where  $\mathbf{E}_{pe}$  is the electric field of the plasma wave oscillating at the eigen frequency  $\omega_{L}(k)$  (see Eq. (8)) and  $\mathbf{E}_{d}$  is the small perturbing driving field operating at  $\omega = \omega_{L}$ . For a driving field of the form:

$$\mathbf{E}_{d} = \hat{\mathbf{e}}_{z} E_{0} F_{p,l}(X) \cos(kz - \omega t + l\theta), \tag{B2}$$

where  $\hat{\mathbf{e}}_z$  is the unit vector in the z-direction, a plasma electric field oscillation will be excited of the form:

$$\mathbf{E}_{pe} = \hat{\mathbf{e}}_z \frac{\omega E_0 t}{2} F_{p,l}(X) \sin(kz - \omega t + l\theta)$$
 (B3)

to a first order approximation  $\omega_{\rm L} \sim \omega_{\rm p}$ .

In practice the frequency of a plasma wave  $\omega_L$  is not exactly equal to the so-called plasma frequency  $\omega_p$  as it is subject to both dispersion in the linear regime, and frequency suppression in the non-linear regime<sup>30</sup>. The driving field must accurately match the plasma wave

frequency to obtain an efficient amplification and avoid the amplification of non-resonant modes. Frequency matching that can be accounted for by Eq. (8) but the non-linear frequency reduction associated with Landau damping in the non-linear regime must be estimated.

For the simulations produced for this manuscript the standard dispersion (Eq. (8)) is sufficient for efficient amplification as the phase speed is so high that any Landau damping that does occur is in the linear regime. This is also the case for the simulations described in previous publications<sup>10,21</sup>.

The estimate used for the driver frequency  $\omega$  in Ref. 22 was  $\omega = 1.11\omega_{\rm p}$  based on preliminary simulations. The driving field was chosen such that the plasma wave should reach a normalized amplitude of  $a_0 = 0.3$  over a time  $t = 10T_p$ .

When performing simulations to observe second order magnetic fields the driving electric field requires not just the longitudinal component but the transverse components as well. If the driver does not contain the transverse field structure discrepancies similar to those seen in the simulation of a standing l=2 wave are observable (see Section III), indicating possible additional non-resonant mode growth.

The driving electric fields are calculated using Eqs. (A2), (A3) and (A4) for the standing helical plasma wave, and Eqs. (14), (15) and (16) for the traveling waves using appropriate values according to the simulation scenario.

## REFERENCES

- <sup>1</sup>L. Allen, M. W. Beijersbergen, R. J. C. Spreeuw, and J. P. Woerdman, Phys. Rev. A 45, 8185 (1992).
- <sup>2</sup>A. M. Yao and M. J. Padgett, Adv. Opt. Photonics 3, 161 (2011).
- <sup>3</sup>A. Longman, C. Salgado, G. Zeraouli, J. I. Apiñaniz, J. A. Pérez-Hernández, M. K. Eltahlawy, L. Volpe, and R. Fedosejevs, Opt. Lett. **45**, 2187 (2020).
- <sup>4</sup>J. Y. Bae, C. Jeon, K. H. Pae, C. M. Kim, H. S. Kim, I. Han, W.-J. Yeo, B. Jeong,
  M. Jeon, D.-H. Lee, D. U. Kim, S. Hyun, H. Hur, K.-S. Lee, G. H. Kim, K. S. Chang,
  I. W. Choi, C. H. Nam, and I. J. Kim, Results in Phys. 19, 103499 (2020).
- <sup>5</sup>S. S. R. Oemrawsingh, J. A. W. van Houwelingen, E. R. Eliel, J. P. Woerdman, E. J. K. Verstegen, J. G. Kloosterboer, and G. W. t. Hooft, Appl. Opt. **43**, 688 (2004).

- <sup>6</sup>R. K. Tyson, M. Scipioni, and J. Viegas, Appl. Opt. **47**, 6300 (2008).
- <sup>7</sup>M. Massari, G. Ruffato, M. Gintoli, F. Ricci, and F. Romanato, Appl. Opt. **54**, 4077 (2015).
- <sup>8</sup>J. T. Mendonça, S. Ali, and B. Thidé, Phys. Plasmas **16**, 112103 (2009).
- <sup>9</sup>J. T. Mendonça, Phys. Plasmas **19**, 112113 (2012).
- <sup>10</sup>D. R. Blackman, R. Nuter, P. Korneev, and V. T. Tikhonchuk, Phys. Rev. E **100**, 013204 (2019).
- <sup>11</sup>Aman-ur-Rehman, S. Ali, and M. Y. Hamza, AIP Advances 8, 045013 (2018), https://doi.org/10.1063/1.5026040.
- <sup>12</sup>H. Lim and S. Lee, Plasma Science and Technology (2021), 10.1088/2058-6272/ac01be.
- <sup>13</sup>S. A. Khan and A. Fukuyama, Physics of Plasmas **28**, 074507 (2021), https://doi.org/10.1063/5.0040579.
- <sup>14</sup>J. Vieira, R. M. G. M. Trines, E. P. Alves, R. A. Fonseca, J. T. Mendonça, R. Bingham, P. Norreys, and L. O. Silva, Phys. Rev. Lett. 117, 265001 (2016).
- <sup>15</sup>S. N. Khonina and I. Golub, Opt. Lett. **41**, 1605 (2016).
- <sup>16</sup>J. Vieira, J. T. Mendonça, and F. Quere, Phys. Rev. Lett. **121**, 054801 (2018).
- <sup>17</sup>J. A. Arteaga, A. Serbeto, K. H. Tsui, and J. T. Mendonça, Phys. Plasmas 25, 123111 (2018).
- $^{18}\mathrm{G}.$  Pariente and F. Quéré, Opt. Lett.  $\mathbf{40},\,2037$  (2015).
- <sup>19</sup>Y. Shi, J. Vieira, R. M. G. M. Trines, R. Bingham, B. F. Shen, and R. J. Kingham, Phys. Rev. Lett. **121**, 145002 (2018).
- <sup>20</sup>J. L. Kline, D. S. Montgomery, B. Bezzerides, J. A. Cobble, D. F. DuBois, R. P. Johnson, H. A. Rose, L. Yin, and H. X. Vu, Phys. Rev. Lett. 94, 175003 (2005).
- <sup>21</sup>D. R. Blackman, R. Nuter, P. Korneev, and V. T. Tikhonchuk, J. Rus. Laser Res. 40, 419 (2019).
- <sup>22</sup>D. R. Blackman, R. Nuter, P. Korneev, and V. T. Tikhonchuk, Phys. Rev. E **102**, 033208 (2020).
- <sup>23</sup>J. T. Mendonça and J. P. S. Bizarro, Plasma Physics and Controlled Fusion 59, 054003 (2017).
- <sup>24</sup>R. Nuter and V. T. Tikhonchuk, Phys. Rev. E **87**, 043109 (2013).
- <sup>25</sup>A. R. Bell and P. Gibbon, Plasma Phys. Control. Fusion **30**, 1319 (1988).
- $^{26}{\rm D.~Beeman,~J.~Comput.~Phys.~\bf 20,~130~(1976)}.$

- <sup>27</sup>V. T. Tikhonchuk, P. Korneev, E. Dmitriev, and R. Nuter, High Energy Density Physics **37**, 100863 (2020).
- $^{28}{\rm R.~L.~Dewar,~Phys.~Fluids~15,~712~(1972)}.$
- <sup>29</sup>G. J. Morales and T. M. O'Neil, Phys. Rev. Lett. **28**, 417 (1972).
- $^{30}\mathrm{N}.$  A. Yampolsky and N. J. Fisch, Phys. Plasmas  $\mathbf{16},\,072104$  (2009).
- <sup>31</sup>S. Brunner and E. J. Valeo, Phys. Rev. Lett. **93**, 145003 (2004).
- <sup>32</sup>H. X. Vu, D. F. DuBois, and B. Bezzerides, Phys. Rev. Lett. **86**, 4306 (2001).
- <sup>33</sup>L. Yin, B. J. Albright, K. J. Bowers, W. Daughton, and H. A. Rose, Phys. Plasmas 15, 013109 (2008).
- <sup>34</sup>L. Yin, B. J. Albright, H. A. Rose, K. J. Bowers, B. Bergen, R. K. Kirkwood, D. E. Hinkel, A. B. Langdon, P. Michel, D. S. Montgomery, and J. L. Kline, Phys. Plasmas 19, 056304 (2012).